lubricants

MDPI

Article

Reducing the Friction Coefficient of Heavy-Load Spherical Bearings in Bridges Using Surface Texturing—A Numerical Study

Qian Hu [1], Qingxiang Pei [1,2] and Pei Li [1,3,*]

[1] Henan International Joint Laboratory of Structural Mechanics and Computational Simulation, School of Architecture and Civil Engineering, Huanghuai University, Zhumadian 463000, China; 20161650@huanghuai.edu.cn (Q.H.); pqx1112@163.com (Q.P.)
[2] College of Architecture and Civil Engineering, Xinyang Normal University, Xinyang 464000, China
[3] Centre for Industrial Mechanics, Institute of Mechanical and Electrical Engineering, University of Southern Denmark, 6400 Sønderborg, Denmark
* Correspondence: lipei@sdu.dk; Tel.: +45-6550-3547

Abstract: Spherical bearings play a crucial role in maintaining the safety of bridge systems. The frequent operation and wear rate over their lifespan highlight the necessity for methods to improve their tribological performance. In this study, GQZ-60000 unidirectionally movable spherical bearings were the research object, and three different surface textures—spherical cap, ellipsoidal cap, and double spherical cap—were incorporated into a curved PTFE surface to enhance its tribological performance, with the major focus being on reducing the friction coefficient. The Jakobsson–Floberg–Olsson cavitation boundary condition was used to solve the Reynolds equation numerically to obtain the elastohydrodynamic lubrication pressure, and the parametric effect of the three textures on the friction coefficient were analyzed. Based on the simulation results, a rational texture with rational geometric values are recommended to obtain the minimum friction coefficient of the bearing. However, it was also found that the deformation of the lubricated surface significantly affects the lubricant film thickness, and cavitation of the lubricant film may also affect the selection of rational textures, especially when the relative sliding velocity between lubricated surfaces is high.

Keywords: spherical bearings; surface texture; elastohydrodynamic lubrication; Reynolds equation; JFO boundary condition; friction coefficient

check for updates

Received: 27 February 2025
Revised: 10 April 2025
Accepted: 11 April 2025
Published: 13 April 2025

Citation: Hu, Q.; Pei, Q.; Li, P. Reducing the Friction Coefficient of Heavy-Load Spherical Bearings in Bridges Using Surface Texturing—A Numerical Study. *Lubricants* **2025**, *13*, 180. https://doi.org/10.3390/lubricants13040180

Copyright: © 2025 by the authors. Licensee MDPI, Basel, Switzerland. This article is an open access article distributed under the terms and conditions of the Creative Commons Attribution (CC BY) license (https://creativecommons.org/licenses/by/4.0/).

1. Introduction

Spherical bearings, commonly used as bridge supports, ensure structural stability and accommodate deformation. They distribute loads and adjust deformations to enhance seismic resistance, contributing to the safe operation and maintenance of bridges. Despite their widespread use, the frequent motion and high wear rate of spherical bearings necessitate research to minimize friction and wear, thereby enhancing performance and extending service life. Consequently, numerous initiatives have aimed to improve the tribological performance of spherical bearings.

To meet the requirements for low friction and high wear resistance, the national standard GB/T 17955-2009 [1] in China specifies that the convex spherical surface of a spherical bearing's convex steel plate may be treated with either stainless steel cladding or hard chrome plating. Additionally, Huang et al. [2] applied ceramic coatings to the friction pairs of bridge bearings, and reported that ceramic-coated friction pairs exhibit excellent friction performance. Zhang [3] designed a highly stable spherical bearing for

bridges using a combination of a spherical PTFE plate and rolling balls to effectively reduce the friction between the upper bearing plate and the middle bracket, preventing excessive wear and extending the device's service life. Wang [4] fabricated CF/GO/PTFE and CNT/GO/PTFE sliding plates via cold pressing and sintering, and demonstrated that CF and CNTs increased the friction coefficient, while GO moderately reduced it. Feng [5] developed a novel steel damping isolation bearing suitable for prefabricated railway bridges, which exhibited excellent low-cycle fatigue performance. Building on this, Song et al. [6] further enhanced the sliding layer with slide-modified UHMWPE, improving wear resistance and load-bearing capacity while reducing bearing wear.

In addition, surface texturing by way of introducing specially designed features on lubricated surfaces [7,8] leads to changes in the lubricant film thickness gradient, and thus can improve the lubrication effect and increase load-bearing capacity [9,10]. Apart from that, surface textures can capture wear particles to reduce wear, even maintaining the consistency of the lubrication film under heavy loads [11]. Thus, this phenomenon has been widely employed to increase tribomechanical components' friction coefficients, wear resistance, and load-bearing capacity [12–14]. The use of surface textures to reduce wear and friction between lubricated surfaces [15] also calls for a thorough grasp of how texture parameters affect lubrication performance [16]. For example, Kovalchenko et al. [17] experimentally demonstrated that using laser-textured dimples can effectively reduce the friction coefficient under boundary lubrication circumstances. Xie et al. [18] conducted experimental research on the tribological performance of triangular textures under water lubrication, and found that a triangular texture exhibited the best friction-reducing effect in the clockwise direction. Li et al. [19] investigated the effect of surface textures on the friction performance of aircraft valves and reported that among the studied textures, the grass-lip texture was the most suitable.

Numerous researchers have also discovered that different textures may have varying effects on lubrication performance [20], and a well-designed texture can effectively reduce the friction coefficient and increase load-bearing capacity. To this end, the performance of parallel sliding bearings with ellipsoidal, triangular, elliptical, spherical, and circular textures was examined by Qiu et al. [21]. Hu et al. [22] conducted a study on the tribological performance of cross-groove textures with different shapes, including triangular, square, hexagonal, and circular. Shen and Khonsari [23] compared optimized groove textures, including those that were rhombic, elliptical, hexagonal, square, and circular, with standard ones, highlighting the former's tribological advantages. These studies are significant in terms of selecting suitable surface textures for bearings used in various situations, while most of them are subjected to light or intermediate load. Under heavy-load conditions, the contact stress on components such as bearings, gears, and sliders increases significantly, exacerbating fatigue and adhesive and abrasive wear. This wear can also be alleviated by manipulating surface texture. Shen et al. [24] found that textured spherical plain bearings exhibited lower friction coefficients than untextured ones. Dang et al. [25] reported that circular pit textures on friction disks improved wear and friction performance. Tang et al. [26] showed that textured gear surfaces had lower friction coefficients. Liu et al. [27] demonstrated that optimized texture distributions enhanced load-bearing capacity and reduced wear. Dong et al. [28] found that circular textures (80 μm and 20 μm) improved lubrication under heavy loads.

In the literature, it is evident that although extensive research has optimized the tribological performance of spherical bearings, the application of surface texturing to improve spherical bearings under heavy loads remains limited. This study investigated three texture types—spherical cap, ellipsoidal cap, and double spherical cap—to enhance the tribological performance of spherical bearings used in bridges. The Reynolds equation

was used to obtain the lubrication film pressure on the lubricated surface of spherical bearings, with elastohydrodynamic lubrication characteristics accounting for deformation under heavy load, and the friction coefficient of the bearing was further derived. Eventually, the rational texture morphology and values of geometrical parameters for achieving the minimum friction coefficient were identified.

2. Lubrication Model

This study considered GQZ-60000 spherical bearings for bridges [1], as shown in Figure 1. The manufacturer of these is Hengshui Jingtong Engineering Rubber Co., Ltd., located in Hengshui City, Hebei Province, China. The bearing capacity is 60,000 kN, and the radius of the curved PTFE surface is 1015 mm. The curved PTFE surface and the convex steel plate are made of polytetrafluoroethylene (PTFE) and 022Cr19Ni13Mo stainless steel, respectively. It should also be noted that for this bearing, the transmission angle of the convex steel plate must not exceed 0.05 rad. When the bridge is subjected to its own and external loads (such as vehicle, wind, and seismic loads), the spherical bearings must facilitate smooth rotation and displacement. As a result, relative motion occurs between the convex steel plate and the curved PTFE surface, which may repeat tens of millions of times over the bearing's service life. Therefore, reducing wear, extending the service life, and enhancing lubrication performance are crucial. As mentioned, introducing surface texturing onto the curved PTFE surface, as adopted in this study, can reduce friction and improve bearing durability. The lubricant film pressure between the convex steel plate and the curved PTFE surface was calculated using the Reynolds equation, accounting for the elastic deformation of the curved PTFE surface. The materials and mechanical properties of the convex steel plate and the curved PTFE surface are detailed in Table 1. In this study, it was assumed that the spherical bearing was subjected to a load of 6000 kN.

Table 1. Materials and mechanical properties of convex steel plate and curved PTFE surface [1].

Part		**Convex Steel Plate**	**Curved PTFE Surface**
Materials		**022 Cr19Ni13Mo3 Stainless Steel**	**Polytetrafluoroethylene**
Mechanical properties	Elasticity modulus (GPa)	195	0.5
	Poisson ratio	0.3	0.4
	Tensile strength (MPa)	480	27.6
	Yield strength (MPa)	177	23
	Hardness (HB)	187	58
Physical properties	Density (g/cm^3)	7.98	2.2
	Tensile strength (MPa)	≥690	≥30
	Elongation at break (%)	≥40	≥300
Frictional properties	Dry friction coefficient	0.1	0.012

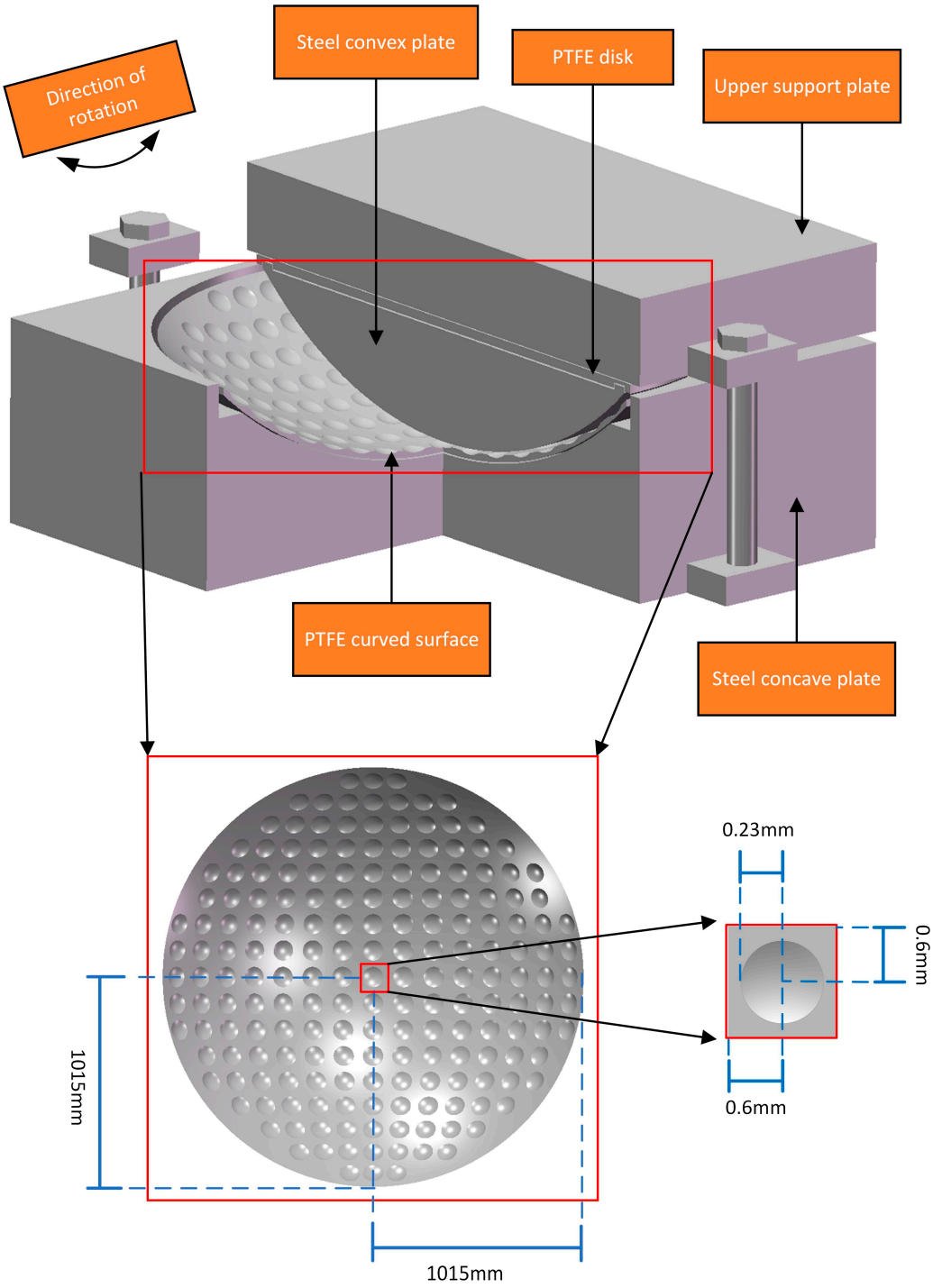


Figure 1. Illustration of the unidirectional movable GQZ-60000 spherical bearings for bridges.

2.1. Reynolds Equation Incorporating the JFO Boundary Condition

In numerical modeling, the PTFE surface was fixed and the convex steel plate was given a circumferential sliding velocity. It was also assumed that the PTFE surface was always separated from the convex steel plate, i.e., contact was not considered in this study. Due to the computational cost, it was almost impossible to simulate the whole curved PTFE surface, which has in total more than 10 thousand textures. Hence, only the central region of the textured PTFE surface was modeled by assuming periodic boundary conditions in this study. Also, it may be noted that for the spherical bearing considered in this study, the curvature radius of the curved PTFE surface was much larger than the radius of its circular edge. Therefore, the curved PTFE surface can be assumed to be flat. As such, it was

not necessary to use the spherical coordinate system in this study, and thus the Reynolds equation for elastohydrodynamic lubrication can be expressed as [29]:

$$\frac{\partial}{\partial x}\left(\frac{\rho h^3}{\eta}\frac{\partial p}{\partial x}\right)+\frac{\partial}{\partial y}\left(\frac{\rho h^3}{\eta}\frac{\partial p}{\partial y}\right)=6u\frac{\partial(\rho h)}{\partial x} \tag{1}$$

where x is the sliding direction between the convex steel plate and curved PTFE surface, y corresponds to the direction perpendicular to x, u represents the sliding velocity of the convex steel plate, η represents the viscosity, ρ represents density of the lubricant, and p denotes the lubricant film pressure. h represents the thickness of the lubricant film between the two lubricated surfaces and can be defined as:

$$h=h_0+h_{tex}+\delta \tag{2}$$

where h_0 represents the referenced lubricant film thickness between nontextured surfaces, h_{tex} is the depth of the surface texture and will be defined later for different textures, and δ is the deformation of the lubricated surface caused by pressure. It is noteworthy that this spherical bearing rotates in only one direction in real applications (see Figure 1), and thus the relative motion between the lubricated surfaces is unidirectional sliding.

Solving the elastohydrodynamic lubrication model using the Reynolds equation requires a proper cavitation boundary condition that governs the rupture of lubrication film. The most commonly applied conditions include Jakobsson–Floberg–Olsson (JFO), Reynolds, half-Sommerfeld, and Sommerfeld boundary conditions. The half-Sommerfeld and Sommerfeld boundary conditions are straightforward to apply; nevertheless, their presumption of a continuous lubricant film throughout the entire fluid domain or half thereof may result in significant inaccuracies. The Reynolds boundary condition assumes film rupture at the point where both the film pressure and the pressure gradient perpendicular to the x-direction equal zero. Although this model offers a more plausible explanation at the lubricant film rupture site, it is unable to adequately explain the lubricant film's reformation. The JFO cavitation boundary condition accurately predicts both the lubrication film rupture location and the boundary for lubricant film reformation and was therefore utilized in this research. The Reynolds equation, reformulated using the JFO cavitation boundary conditions, can be expressed as follows [30]:

$$\frac{\partial}{\partial x}\left(\frac{\rho h^3}{\eta}\frac{\partial p}{\partial x}\right)+\frac{\partial}{\partial y}\left(\frac{\rho h^3}{\eta}\frac{\partial p}{\partial y}\right)=6u\frac{\partial(\rho h\theta)}{\partial x} \tag{3}$$

where θ represents the density ratio of lubricating silicone grease, which can be expressed as: $\theta=1+(1-S)\Phi$. In this setting, S denotes the cavitation index, which is expressed as follows:

$$S=\begin{cases}0, & \Phi\le 0\\ 1, & \Phi>0\end{cases} \tag{4}$$

where Φ denotes a dimensionless dependent parameter, defined by $p/p_0=S\Phi$, where p_0 represents the standard atmospheric pressure.

For the convergence of numerical calculations, parameters in the Reynolds equation are usually nondimensionalized as follows:

$$H=\frac{h}{h_0},\ P=\frac{p}{p_0}, P=S\Phi,\ \rho'=\frac{\rho}{\rho_0},\ \eta'=\frac{\eta}{\eta_0},\ Y=\frac{y}{L_y},\ X=\frac{x}{L_x},\ \Lambda=\frac{6u\eta_0 Lx}{h_0^2(p-p_0)}, \alpha=\frac{L_x}{L_y} \tag{5}$$

where H is the dimensionless lubricant film thickness, P denotes the dimensionless pressure, X and Y represent the dimensionless coordinates in the x and y directions, respectively,

and L_x and L_y are the length and width of the texture's unit cell, respectively. Substituting Equation (5) into Equation (3) yields the nondimensional Reynolds equation:

$$\frac{\partial}{\partial X}\left(\frac{\rho' H^3}{\eta'}\frac{\partial(S\Phi)}{\partial X}\right)+\alpha^2\frac{\partial}{\partial Y}\left(\frac{\rho' H^3}{\eta'}\frac{\partial(S\Phi)}{\partial Y}\right)=\Lambda\frac{\partial((1+(1-S)\Phi)\rho' H)}{\partial X} \tag{6}$$

Obtaining an analytical solution to the elliptic partial differential equation in Equation (6) is highly challenging; hence, numerical methods are typically employed to solve elliptic partial differential equations, such as the finite difference method (FDM) [31], boundary element method [32–34], and finite element method [35–37]. The FDM is frequently used to solve the Reynolds equation, and was also adopted in this study with a central difference scheme to compute the partial derivatives. Then, the nondimensional Reynolds equation (Equation (6)) can be discretized as:

$$A_{i,j}\Phi_{i,j}-B_{i,j}\Phi_{i-1,j}S_{i-1,j}-C_{i,j}\Phi_{i+1,j}S_{i+1,j}-D_{i,j}\Phi_{i,j-1}S_{i,j-1}-E_{i,j}\Phi_{i,j+1}S_{i,j+1}=-F_{i,j} \tag{7}$$

where:

$$\begin{aligned}
B_{i,j}&=\frac{\rho'_{i-1/2,j}H^3_{i-1/2,j}}{\eta'_{i-1/2,j}\Delta X^2}=\frac{\left(\rho'_{i-1,j}+\rho'_{i,j}\right)\left(H_{i-1,j}+H_{i,j}\right)^3}{8\left(\eta'_{i-1,j}+\eta'_{i,j}\right)\Delta X^2}\\
C_{i,j}&=\frac{\rho'_{i+1/2,j}H^3_{i+1/2,j}}{\eta'_{i+1/2,j}\Delta X^2}=\frac{\left(\rho'_{i+1,j}+\rho'_{i,j}\right)\left(H_{i+1,j}+H_{i,j}\right)^3}{8\left(\eta'_{i+1,j}+\eta'_{i,j}\right)\Delta X^2}\\
D_{i,j}&=\alpha^2\frac{\rho'_{i,j-1/2}H^3_{i,j-1/2}}{\eta'_{i,j-1/2}\Delta Y^2}=\alpha^2\frac{\left(\rho'_{i,j-1}+\rho'_{i,j}\right)\left(H_{i,j-1}+H_{i,j}\right)^3}{8\left(\eta'_{i,j-1}+\eta'_{i,j}\right)\Delta Y^2}\\
E_{i,j}&=\alpha^2\frac{\rho'_{i,j+1/2}H^3_{i,j+1/2}}{\eta'_{i,j+1/2}\Delta Y^2}=\alpha^2\frac{\left(\rho'_{i,j+1}+\rho'_{i,j}\right)\left(H_{i,j+1}+H_{i,j}\right)^3}{8\left(\eta'_{i,j+1}+\eta'_{i,j}\right)\Delta Y^2}\\
A_{i,j}&=\left(B_{i,j}+C_{i,j}+D_{i,j}+E_{i,j}\right)S_{i,j}+\frac{\Lambda\left(1-S_{i,j}\right)\rho'_{i,j}H_{i,j}}{\Delta X}\\
F_{i,j}&=\frac{\Lambda}{\Delta X}\left(H_{i,j}-H_{i-1,j}-\left(1-S_{i-1,j}\right)\Phi_{i-1,j}\rho'_{i,j}H_{i-1,j}\right)
\end{aligned} \tag{8}$$

where A, B, C, D, E, F represent coefficient matrices, ΔX refers to the distances in x directions between two neighboring nodes, and ΔY refers to the distances in y directions between two neighboring nodes. The computational domain can be divided into a uniformly spaced grid, with nodes in the x-direction labeled m and nodes in the y-direction labeled n. Therefore, the total number of nodes in the entire computational domain is $m \times n$.

2.2. Lubricant Density and Viscosity, and Deformation of PTFE Surface

Due to the heavy loads supported by the spherical bearing in actual applications (i.e., bridges), both the convex steel plate and the curved PTFE surface will deform, but deformation of the latter is more significant due to its much lower elastic modulus. In this study, only the elastic deformation of the curved PTFE surface was considered. Furthermore, the density and viscosity of the lubricant vary as the lubricant film pressure changes.

In this study, the following relationship between density and pressure was used [38]:

$$\rho'=\rho_0\left(1+\frac{0.6\times10^{-9}p}{1+1.7\times10^{-9}p}\right) \tag{9}$$

where ρ' represents the lubricant density at pressure p and ρ_0 is the density at atmospheric pressure. The viscosity–pressure relationship is described as [39]:

$$\eta'=\eta_0 e^{\kappa\cdot p} \tag{10}$$

where η' represents the lubricant viscosity at pressure p, η_0 is the viscosity at atmospheric pressure, and κ is the pressure–viscosity coefficient.

Deformation of the curved PTFE surface is obtained using the Winkler elastic foundation model shown in Figure 2. The contact pressure of each spring can be expressed as [40]:

$$p_{i,j} = \frac{E_W}{L_{i,j}} \delta_{i,j} \tag{11}$$

where $\delta_{i,j}$ represents the deformation at node $(i,\ j)$, $p_{i,j}$ is the lubrication pressure, $L_{i,j}$ is the thickness of the elastic layer, and E_W is the equivalent elastic modulus, expressed as:

$$E_w = \left[\frac{1 - v_1^2}{E_1} - \frac{1 - v_2^2}{E_2} \right]^{-1} \tag{12}$$

where E_1, v_1 and E_2, v_2 are the elastic moduli and Poisson's ratios of the convex steel plate and curved PTFE surface, respectively.

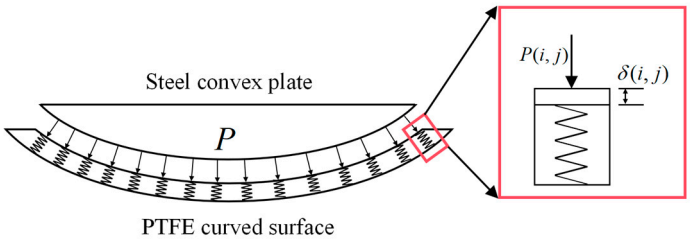


Figure 2. Schematic diagram of the Winkler elastic foundation model.

2.3. Computational Algorithm

Solving the lubrication model represented by the Reynolds equation in Section 2.1 will yield the lubrication pressure, which can further derive the lubrication performance. For the textured spherical bridge bearing in this study, the lubricant film thickness in the Reynolds equation is a summation of the referenced lubricant film thickness, the depth of the surface texture and the deformation of the lubricated surface (see Equation (2)). The depth of the surface texture is defined by the geometric model in Section 3.1, while deformation of the lubricated surface is computed from the lubrication pressure via the Winkler model in Section 2.2. Hence, the Reynolds equation needs to be solved iteratively, which is detailed as follows.

The discretized Reynolds equation (see Equation (7)) can be rewritten as the following iterative form:

$$\Phi_{i,j}^{k+1} = \frac{-F_{i,j} + B_{i,j}\Phi_{i-1,j}^{k+1}S_{i-1,j}^{k+1} + D_{i,j}\Phi_{i,j-1}^{k+1}S_{i,j-1}^{k+1} + C_{i,j}\Phi_{i+1,j}^{k}S_{i+1,j}^{k} + E_{i,j}\Phi_{i,j+1}^{k}S_{i,j+1}^{k}}{A_{i,j}} \tag{13}$$

where k refers to the iteration step and $(\cdot)_{i,j}^{k}$ refers to the value of $(\cdot)$ at node (i, j) during the k-th iteration step. To accelerate the iterative convergence of the numerical solution, the successive over-relaxation (SOR) method can be employed as follows:

$$\Phi_{i,j}^{k+1} = (1-\beta)\Phi_{i,j}^{k} + \beta \frac{-F_{i,j} + B_{i,j}\Phi_{i-1,j}^{k+1}S_{i-1,j}^{k+1} + D_{i,j}\Phi_{i,j-1}^{k+1}S_{i,j-1}^{k+1} + C_{i,j}\Phi_{i+1,j}^{k}S_{i+1,j}^{k} + E_{i,j}\Phi_{i,j+1}^{k}S_{i,j+1}^{k}}{A_{i,j}} \tag{14}$$

where β denotes the super-relaxation coefficient, which is set to be 1–2, and in this paper 1.95. The iteration is deemed convergent when the following requirement is fulfilled:

$$\frac{\sum_{i=1}^{m}\sum_{j=1}^{n}\left|\Phi^{k+1}-\Phi^{k}\right|}{\sum_{i=1}^{m}\sum_{j=1}^{n}\Phi^{k+1}}<1\times10^{-6} \tag{15}$$

After calculating Φ, one can derive S using Equation (4), and P can be determined from Equation (5).

By integrating $p(x,y)$ across the whole computational domain, the load-bearing capacity W of the lubrication film between the lubricated surfaces can be determined, and is defined as:

$$W=\iint p(x,y)dxdy \tag{16}$$

When the following conditions are met, the bearing capacity can be considered to meet the load conditions:

$$\frac{(F-W)}{F}\leq1\times10^{-4} \tag{17}$$

where F represents the load borne by the modeled region of the spherical bearing, which can be expressed as:

$$F=W_b\times\frac{S_s}{S_c} \tag{18}$$

where $W_b=6\times10^6$ is the total load applied to the spherical bearing, S_s represents the area of the simulated domain, S_c represents the total area of the lubricated surface, and $S_c=1.64\,\mathrm{m}^2$. If Equation (17) is not satisfied, the lubricant film thickness should be adjusted as follows: $h_0=h_0+0.5\times h_0\times(W/F-1)$, and Equations (5)–(17) recalculated. This process is repeated iteratively until Equation (17) is met.

2.4. Friction Coefficient

For bridge spherical bearings, when the load-bearing capacity requirements are met, the focus is often on reducing wear to extend service life. A lower coefficient of friction generally leads to reduced energy loss and wear. Therefore, the coefficient of friction is used here as the criterion to assess the friction performance of spherical bearings, as defined below. Specifically, the friction coefficient is defined as the ratio of the integral of the tangential stress on the lubricated surface to the normal load-carrying capacity within the computational domain:

$$\mu=\frac{f}{W} \tag{19}$$

where f refers to the friction, which can be expressed as:

$$f=\iint\tau(x,y)dxdy \tag{20}$$

where $\tau(x,y)$ refers to the shear stress, which can be expressed as:

$$\tau(x,y)=-\frac{h}{2}\frac{\partial p}{\partial x}+\frac{\eta}{h}u \tag{21}$$

It may be noted that the friction coefficient defined here refers to the lubricant induced friction coefficient rather than the dry friction coefficient of the bearing's material in Table 1.

2.5. Numerical Implementation

The numerical model detailed in Sections 2.1–2.4 was finally solved using self-developed MATLAB (2023b) codes, following the flowchart in Figure 3. The codes were run

on a Dell computer with 36 GB RAM and an Intel (R) Core (TM) i5-8300H CPU purchased from JD.com.

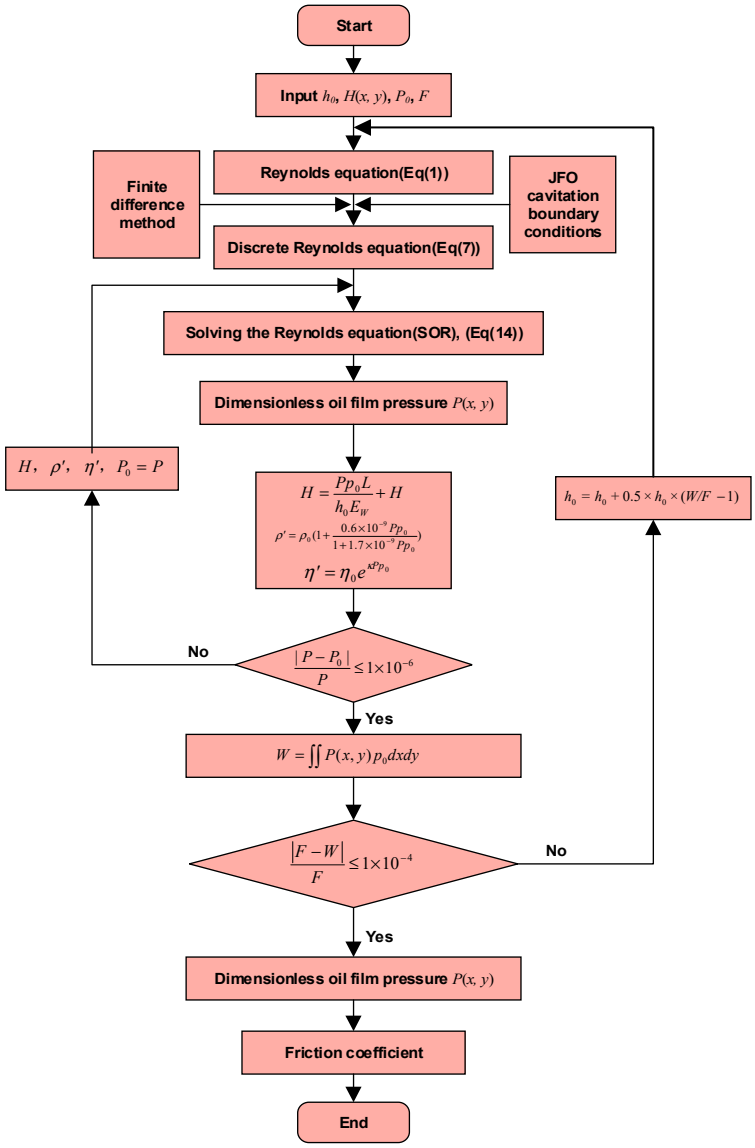


Figure 3. Flowchart for selection of rational surface texture parameters.

3. Modeling of Surface Textures

This study examined three distinct surface textures—spherical cap, ellipsoidal cap, and double spherical cap—aiming to enhance the tribological performance of spherical bearings. The modeling of these surface textures is detailed as follows.

3.1. Texture Models

Figure 1 illustrates the even distribution of the surface texture over the curved PTFE surface. To provide a more intuitive demonstration of the surface textures, the cells of each type of surface texture will be described in detail below.

3.1.1. Spherical Cap

The spherical cap texture on the surface of the curved PTFE surface is shown in Figure 4. In Figure 4a, the lower part depicts a unit cell of the texture on the surface of the curved PTFE surface, whereas the upper part, represented as a rectangular plate, corresponds to the simplified convex steel plate. Figure 4b presents a three-view of this

texture., and Figure 4c shows the equivalent 3D model. In the diagram, d refers to the texture depth, r refers to the texture radius, and h_0 refers to the gap between the nontextured regions of the lubricated surfaces.

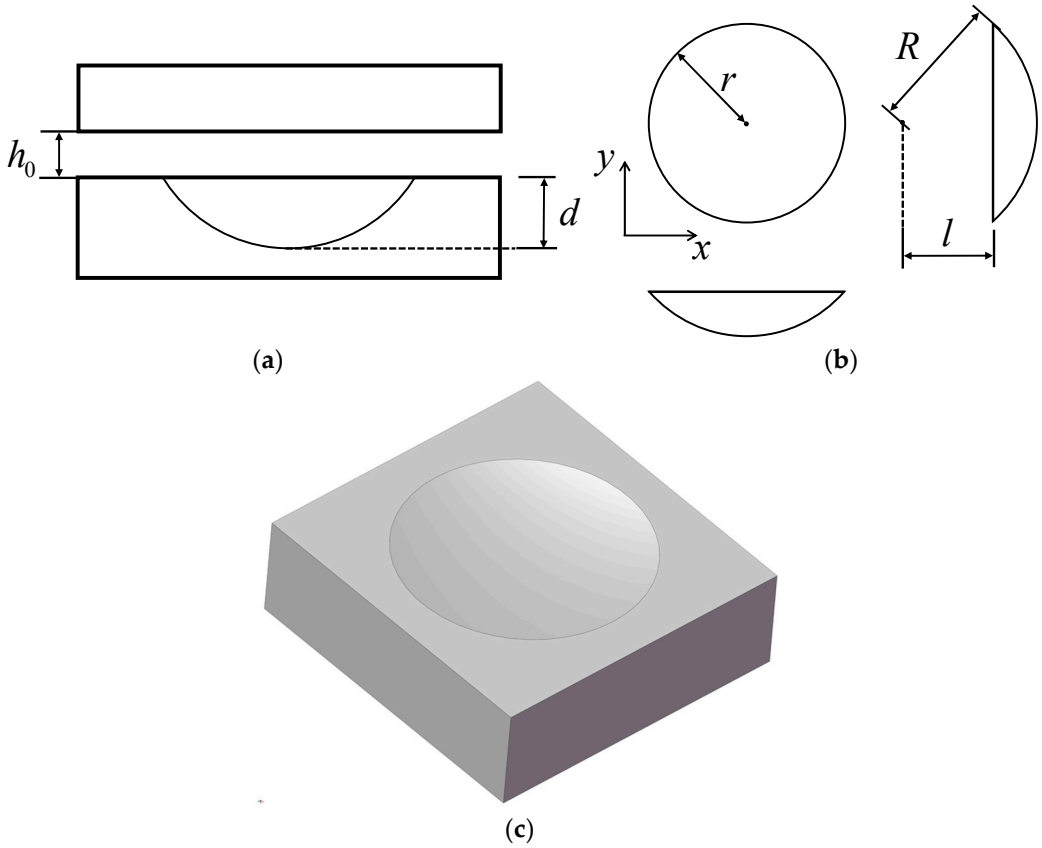


Figure 4. Spherical cap texture: (**a**) section view; (**b**) three-view; (**c**) 3D model.

The radius of the sphere cap of the texture can be written as:

$$R = \frac{(r^2 + d^2)}{2d} \tag{22}$$

The distance l from the centre of the sphere cap to the lower lubricated surface is:

$$l = \sqrt{R^2 - r^2} \tag{23}$$

Thus, the lubricant film thickness h between the lubricated surfaces can be expressed as:

$$h_{tex} = \begin{cases} \left(\sqrt{R^2 - \left((x - x_0)^2 + (y - y_0)^2\right)} - l\right), \ (x - x_0)^2 + (y - y_0)^2 \leq r^2 \\ 0, \ otherwise \end{cases} \tag{24}$$

where (x_0, y_0) represents the coordinates of the cap base center.

3.1.2. Ellipsoidal Cap

The ellipsoidal cap texture is shown in Figure 5. Figure 5a–c present the section view of the texture, three-view of the texture, and the equivalent 3D model, respectively.

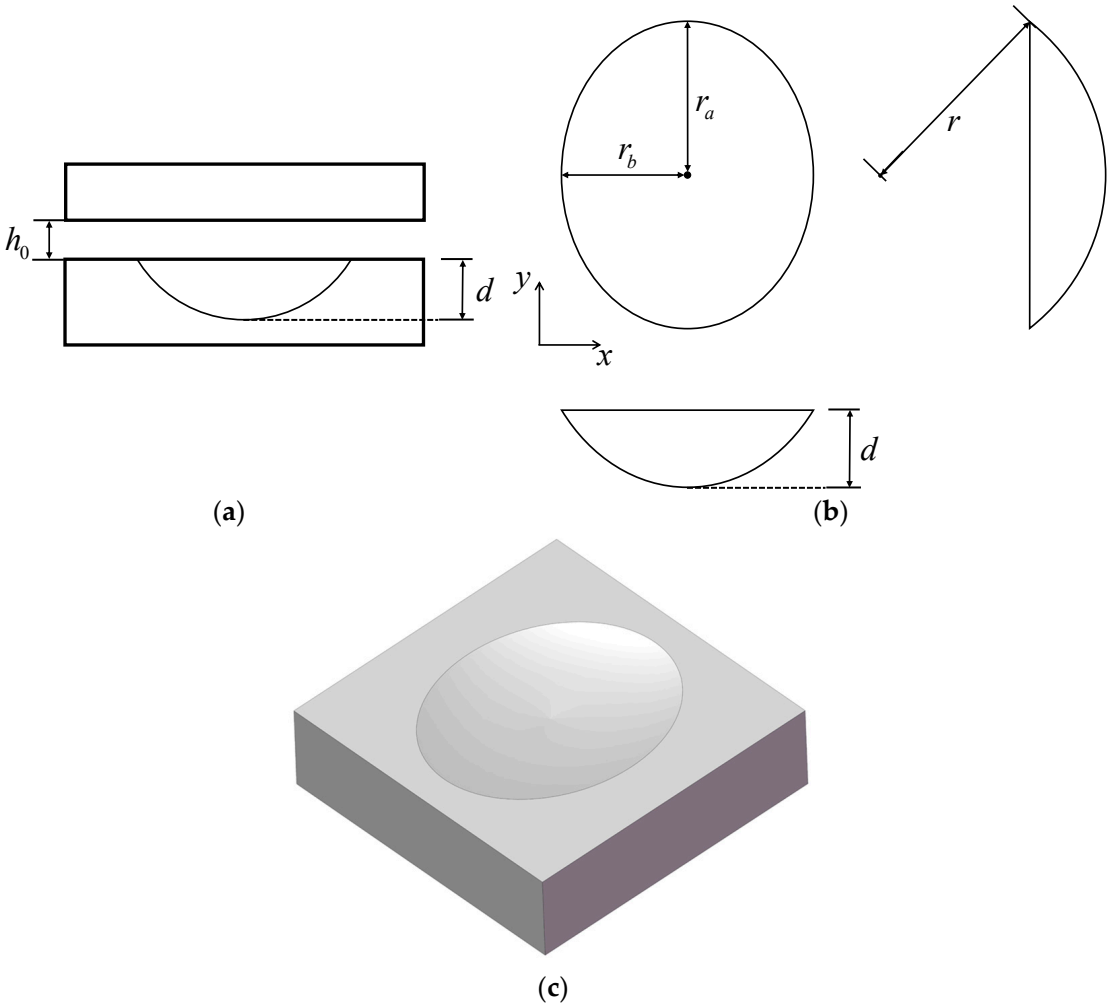


Figure 5. Ellipsoidal cap texture: (**a**) section view; (**b**) three-view; (**c**) 3D model.

The ellipsoidal cap corresponding to the ellipsoid equation can be expressed as:

$$\frac{(x-x_0)^2}{a^2}+\frac{(y-y_0)^2}{b^2}+\frac{\left(z+\sqrt{r^2-{r_a}^2}\right)^2}{c^2}=1 \tag{25}$$

where (x_0, y_0) refers to the center of the ellipsoidal cap base, and:

$$\begin{aligned} c &= d+\sqrt{r^2-{r_a}^2} \\ a &= r_a\frac{c}{\sqrt{c^2-r^2+{r_b}^2}} \\ b &= r_b\frac{c}{\sqrt{c^2-r^2+{r_b}^2}} \end{aligned} \tag{26}$$

where a, b, c refer to the short, medium, and long semi-axes, respectively, of the ellipsoid corresponding to the ellipsoidal cap. r_a represents the major semiaxis of the ellipsoidal cap, r_b represents the minor semiaxis of the ellipsoidal cap, and d refers to the texture depth.

Thus, the lubricant film thickness h between the lubricated surfaces can be expressed as:

$$h_{tex}=\begin{cases} \left(\sqrt{c^2\left(1-\left(\frac{x-x_0}{a}\right)^2-\left(\frac{y-y_0}{b}\right)^2\right)}-\sqrt{r^2-{r_a}^2}\right), \left(\frac{x-x_0}{a}\right)^2+\left(\frac{y-y_0}{b}\right)^2\le r^2 \\ 0, \ otherwise \end{cases} \tag{27}$$

3.1.3. Double Spherical Cap

The double spherical cap texture is shown in Figure 6. Figure 6a–c present the section view of the texture, three-view of the texture, and the equivalent 3D model, respectively.

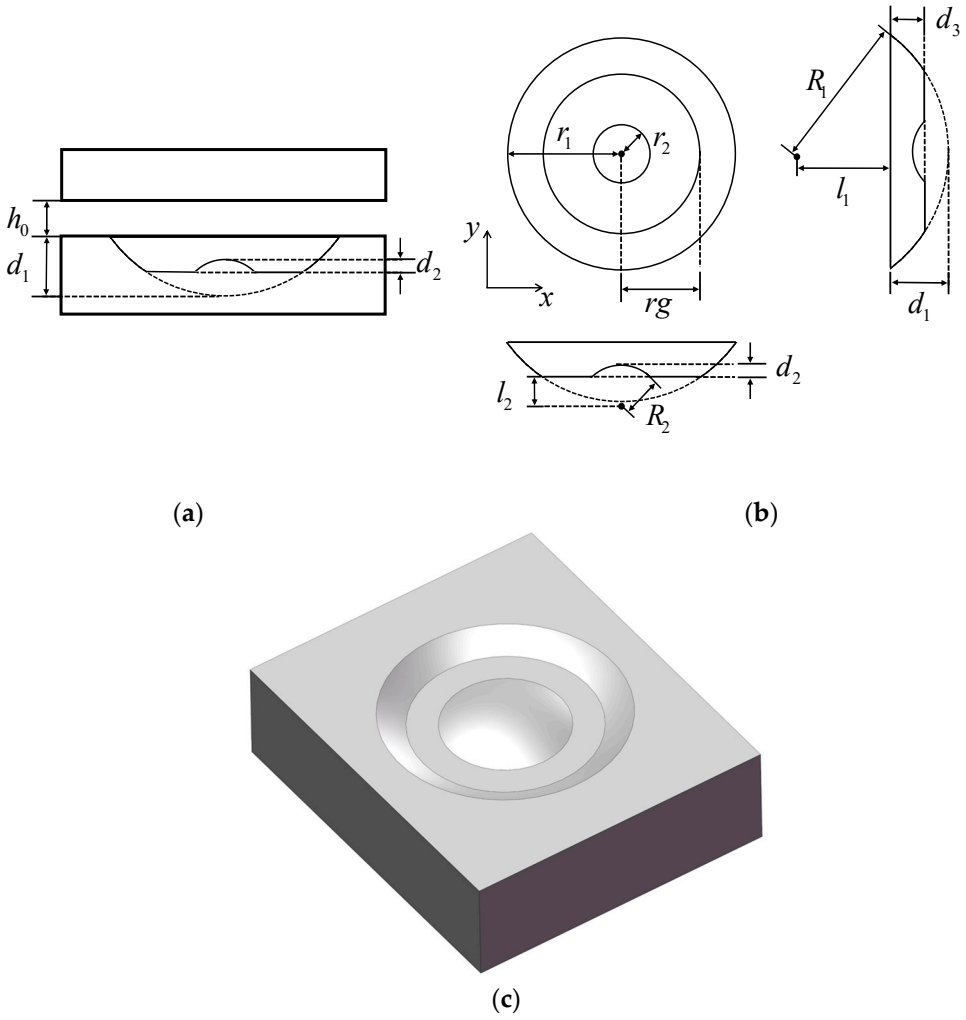


Figure 6. Double spherical cap texture: (**a**) section view; (**b**) three-view; (**c**) 3D model.

In the diagram, r_1, d_1 and r_2, d_2 denote the cap base radii and depth of the larger and smaller spherical caps, respectively. d_3 denotes the depth of the flat platform, which has a radius of rg. The radii of the large and small spherical cap can be expressed as:

$$\begin{aligned} R_1 &= \frac{\left({r_1}^2+{d_1}^2\right)}{2d_1} \\ R_2 &= \frac{\left({r_2}^2+{d_2}^2\right)}{2d_2} \end{aligned} \tag{28}$$

The distance l_1 from the centre of the larger spherical cap to the lower lubricated surface is:

$$l_1 = \sqrt{{R_1}^2 - {r_1}^2} \tag{29}$$

The distance l_2 from the centre of the smaller spherical cap to the flat platform of the texture is:

$$l_2 = \sqrt{{R_2}^2 - {r_2}^2} \tag{30}$$

The radius of the flat platform of the texture is:

$$rg = {R_1}^2 - (d_3 + l_1)^2 \tag{31}$$

Thus, the lubricant film thickness h between the lubricated surfaces can be expressed as:

$$h_{tex} = \begin{cases} \left(d_3 + l_2 - \sqrt{{R_2}^2 - (x - x_0)^2 - (y - y_0)^2} \right), \ (x - x_0)^2 + (y - y_0)^2 < {r_2}^2 \\ d_3, \ {r_2}^2 \le (x - x_0)^2 + (y - y_0)^2 < rg^2 \\ \left(\sqrt{{R_1}^2 - (x - x_0)^2 - (y - y_0)^2} - l_1 \right), \ rg^2 \le (x - x_0)^2 + (y - y_0)^2 < {r_1}^2 \\ 0, \ otherwise \end{cases} \tag{32}$$

where (x_0, y_0) refers to the center coordinates of the larger cap base.

3.2. Arrangements of Numerical Simulations

Since the unit cells of the texture are evenly distributed across the curved PTFE surfaces in the spherical bearings, and it is almost impossible to model the numerous texture cells due to unmanageable computational cost. Only a small region (i.e., 3×3 array of unit cells) of the lubricated surfaces was modeled by applying periodic boundary conditions, as shown in Figure 7.

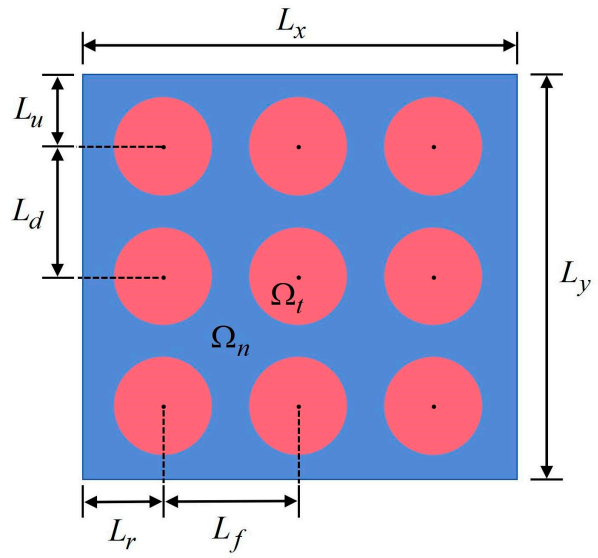


Figure 7. Surface texture's geometric parameters, exemplified by a spherical cap texture.

In the diagram, Ω_t refers to the textured regions, shown in red. Ω_n refers to the untextured region, shown in blue. The distances L_f in the x-direction and L_d in the y-direction between two unit cells are defined as follows:

$$L_f = \frac{L_x}{N_n} \tag{33}$$

$$L_d = \frac{L_y}{N_m} \tag{34}$$

where N_n and N_m refer to the number of surface textures along the x-direction and y-direction of the simulated lubricated surface, respectively. L_x and L_y represent the lengths

of the modeling region in the x-direction and y-direction, respectively. The distance from the boundary cell to the boundary can be described by L_u and L_r:

$$\begin{aligned} L_u &= \frac{L_x}{2N_n} \\ L_r &= \frac{L_y}{2N_m} \end{aligned} \tag{35}$$

For the periodic region (Figure 7) modeled in this study, these two parameters, L_u and L_r are not needed in numerical modeling or computation.

The center $(x_0,\ y_0)$ of each unit cell is:

$$\begin{cases} x_0 = \frac{(2N_i-1)}{N_n+1} \times L_x \ (1 \le N_i \le N_n) \\ y_0 = \frac{(2N_j-1)}{N_m+1} \times L_y \ (1 \le N_j \le N_m) \end{cases} \tag{36}$$

where N_i refers to the N_i-th texture in the x-direction and N_j refers to the N_j-th texture in the y-direction.

4. Results and Discussion

4.1. Verification of Convergence of Lubrication Model

Verifying the convergence of numerical simulation is essential for the parametric selection of surface textures. To achieve this, different numbers of grid nodes (ranging from 50 to 350 along the edge) were used to simulate one cell of the spherical cap texture (see Figure 8). Periodic boundary conditions were applied to the boundaries of the simulated region. Premium-grade 5201-2 lubricating silicone grease was used as the lubricant in this investigation. This grease was chosen due to its excellent oxidation stability and anti-wear properties, which make it suitable for the lubrication requirements of spherical bearings under heavy load. Values for all other parameters needed for the simulation are listed in Table 2. Since the area of the simulated domain $S_s = 4.9 \times 10^{-7}$ m^2 and the total area of the PTFE surface $S_c = 1.64$ m^2, the load $F = 1.79$ N (see Equation (18)).

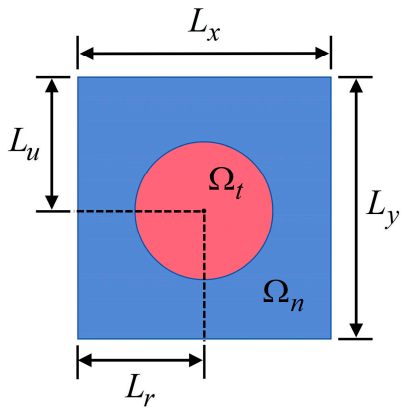


Figure 8. A unit cell model of spherical cap texturing for numerical simulation validation of convergence.

By iteratively solving the Reynolds equation detailed in Section 2, the lubricant film thickness and friction coefficient were obtained, and these are depicted in Figure 9. The figure shows that when the number of edge nodes exceeds 250, variations in the referenced lubricant film thickness and friction coefficient become insignificant, suggesting that the numerical method is reliable. Figure 10 shows that the difference in elastic deformation of textures corresponding to the edge node numbers of 250 and 350 is negligible, which once again demonstrates the reliability of the method. Consequently, 250 edge nodes were

utilized for all subsequent numerical simulations. In addition, the simulation time using the number of nodes was 213.3 s.

Table 2. Simulation parameters.

Texture Parameters	Unit	Parameter Value
Load	N	1.79
Relative velocity between lubricated surfaces u	m/s	0.008
Lubricant viscosity η_0	Pa·s	821
Lubricant density ρ_0	kg/m^3	3400
Pressure–viscosity coefficient κ	m^2/N	2×10^{-8}
Clearance between surfaces h_0	μm	10
Width of the modeled region L_y	μm	700
Length of the modeled region L_x	μm	700
Thickness of the elastic layer L	μm	1000
Spherical cap radius r	μm	200
Spherical cap depth d	μm	15

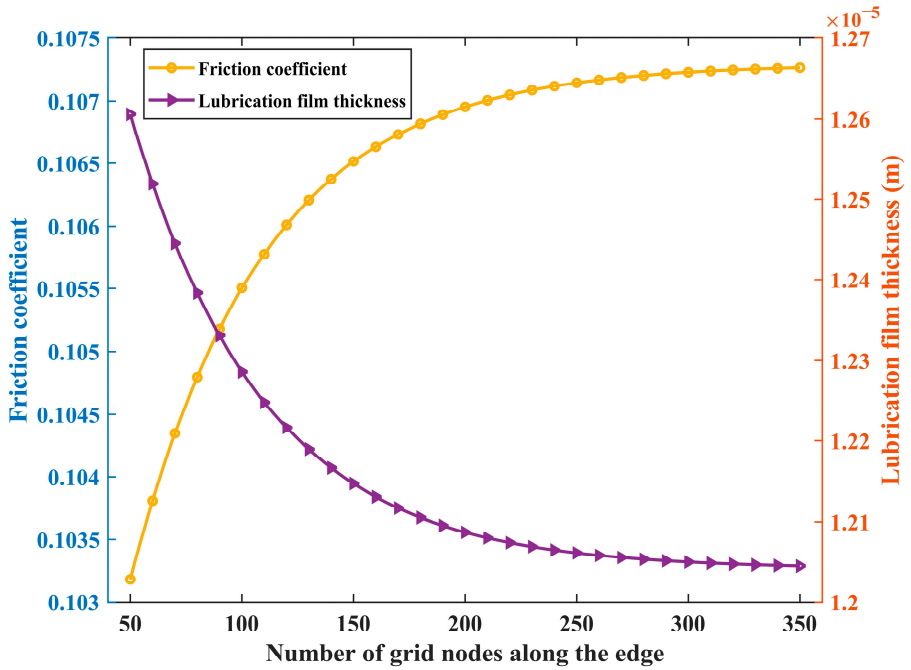


Figure 9. Convergence of numerical outcomes with respect to the number of grid nodes.

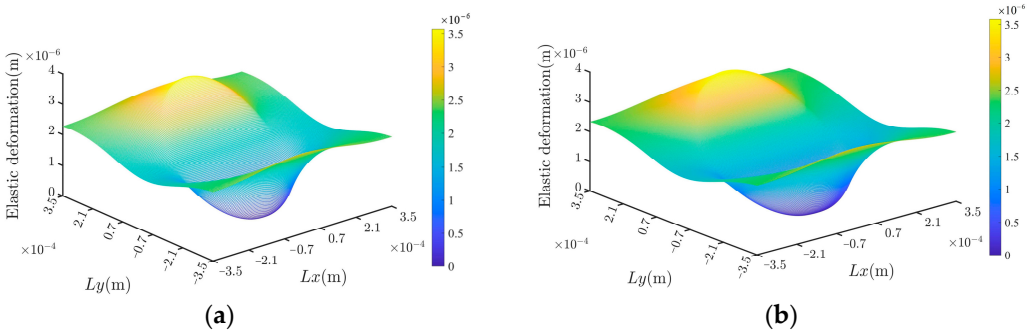


Figure 10. Elastic deformation of the spherical cap texture cell when the number of grid nodes is 250 and 350: (**a**) 250; (**b**) 350.

4.2. Selection of Geometric Parameters

In this work, the simulated region's width L_x and length L_y were set to be 2000 μm (see Figure 7). Since the area of the simulated domain $S_s = 4 \times 10^{-6}$ m^2 and the total area

of the PTFE surface $S_c = 1.64$ m^2, the load $F = 14.64$ N (see Equation (18)). The lubricant viscosity η_0, density ρ_0, clearance h_0, and relative velocity u between the two lubricated surfaces assume the same values as in Table 2.

Table 3 concludes each texture's geometric parameters. Each geometric parameter for the spherical cap texture was assigned five different values, resulting in 25 numerical simulations. In general, more numerical simulations are required for textures with more geometric parameters. In this study, 324 numerical simulations for the double spherical cap texture and 625 simulations for the ellipsoidal cap texture were carried out (see Table 3).

Table 3. Surface texture geometric parameters.

Texture Type	Geometric Parameter (μm)	Value
Spherical cap	r	190, 200, 210, 220, 230
	d	9, 10, 11, 12, 13
Ellipsoidal cap	r_a	190, 200, 210, 220, 230
	r_b	190, 200, 210, 220, 230
	r	600, 700, 800, 900, 1000
	d	9, 10, 11, 12, 13
Double spherical cap	r_1	220, 230, 240
	r_2	70, 80, 90
	d_1	11, 12, 13
	d_2	3, 4, 5
	d_3	6, 7, 8

After obtaining all the numerical simulation results, the spherical bearings' tribological performance, i.e., the friction coefficient defined in Section 2.2, can be analyzed. For example, the impact of the spherical cap texture's parameters, r and d, on the friction coefficient and lubricant film thickness is shown in Figure 11. When the spherical cap radius r remains constant, the friction coefficient decreases as the spherical cap depth d increases and the lubricant film thickness increases as the spherical cap depth d increases. When the spherical cap depth d remains constant, the friction coefficient decreases as the spherical cap radius r increases. When the spherical cap depth $d = [9,\ 11]$ μm, the lubricant film thickness increases and then decreases as the spherical cap radius r increases. When the spherical cap depth $d = [11,\ 13]$ μm, the lubricant film thickness increases as the spherical cap radius r increases. This suggests that of the two geometric parameters' predetermined values, $r = 230$ μm and $d = 13$ μm are the best values.

Additionally, as shown in Figure 11a, the friction coefficient's absolute gradient continuously decreases with the increase in texture depth d. Based on this observation, it can be inferred that the rational texture depth d may be greater than 13 μm. It can be observed in the figure that the texture radius r also exhibits a similar trend between 190 and 230 μm. However, owing to the model's size constraints, as illustrated in Figure 7, when the texture radius r reaches 230 μm, the distance between the adjacent textures becomes very small, limiting the possibility of determining the rational value of the texture radius r using the same approach as for the texture depth d. Therefore, the texture radius r was restricted to 230 μm while the value range of d was further expanded to $[14,\ 44]$ μm. In Figure 12, it can be observed that the texture depth d corresponding to the minimum friction coefficient is 36 μm, but that corresponding to the maximum value of the referenced lubricant film thickness (i.e., h_0 in Equation (1)) is 24 μm. In actual applications, the rational value of d needs to be selected depending on the relative importance of the friction coefficient and lubricant film thickness. In this study, the friction coefficient was of more interest, and thus the rational value of d is 36 μm.

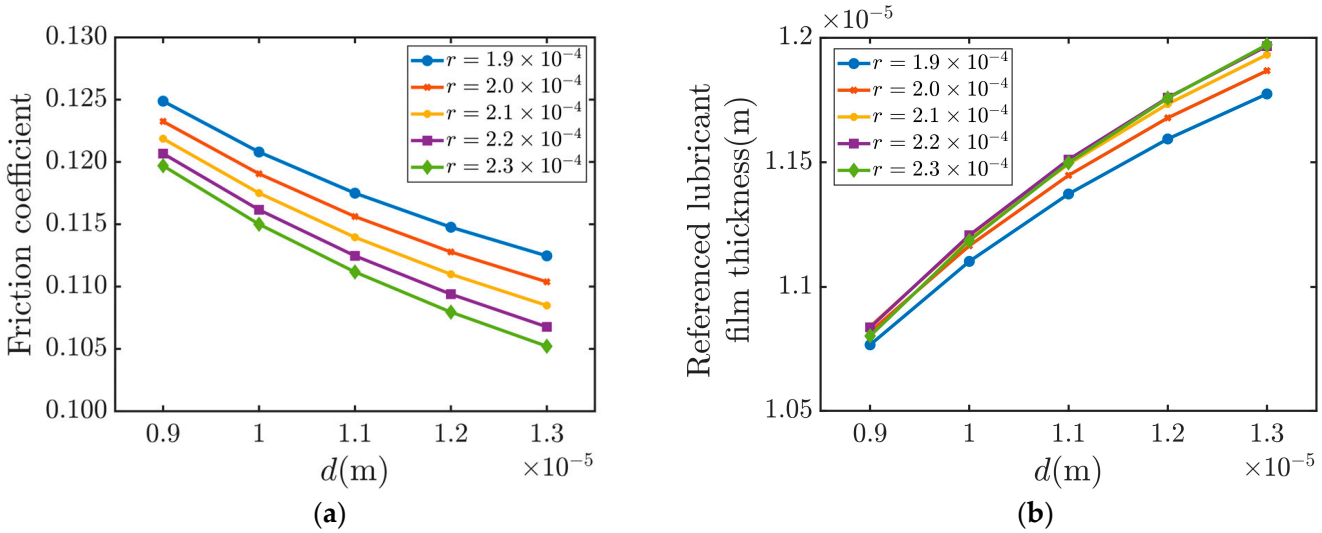


Figure 11. Effect of the texture radius r and texture depth d on the friction coefficient and lubricant film thickness: (**a**) friction coefficient; (**b**) referenced lubricant film thickness.

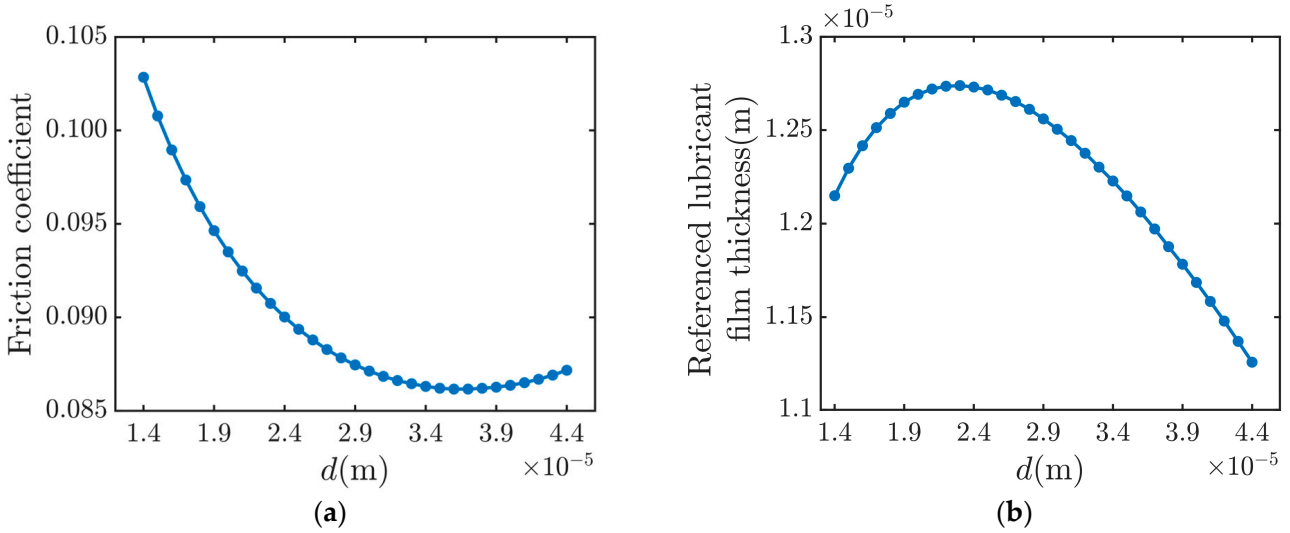


Figure 12. Effect of texture depth d in the expanded range on friction coefficient and lubricant film thickness. Texture radius $r = 230$ μm. (**a**) Friction coefficient; (**b**) referenced lubricant film thickness.

The friction coefficients obtained from all 56 simulations for the spherical texture are presented in Table 4. This dataset consists of two modules: the initial 25 data groups represent results derived from basic geometric parameters, while the subsequent 31 data groups reflect outcomes from an expanded range of the parameter d. It is clearly shown that the minimum value of friction coefficient is 0.08615.

Table 4. Values of tribological parameters corresponding to different values of geometric parameters for the spherical texture.

Underlying geometric parameters					
Geometric parameters		μ	Geometric parameters		μ
r (μm)	d (μm)		r (μm)	d (μm)	
190	9	0.12488	210	12	0.11099
	10	0.12080		13	0.10848
	11	0.11750	220	9	0.12067
	12	0.11476		10	0.11616
	13	0.11246		11	0.11247
200	9	0.12325		12	0.10939
	10	0.11905		13	0.10677
	11	0.11562	230	9	0.11969
	12	0.11278		10	0.11500
	13	0.11038		11	0.11117
210	9	0.12186		12	0.10795
	10	0.11750		13	0.10520
	11	0.11395			
Expanded geometric parameters					
Geometric parameters		μ	Geometric parameters		μ
r (μm)	d (μm)		r (μm)	d (μm)	
230	14	0.10284	230	30	0.08712
	15	0.10077		31	0.08684
	16	0.09895		32	0.08662
	17	0.09735		33	0.08645
	18	0.09592		34	0.08630
	19	0.09464		35	0.08621
	20	0.09350		36	0.08615
	21	0.09248		37	0.08616
	22	0.09156		38	0.08620
	23	0.09074		39	0.08626
	24	0.09002		40	0.08636
	25	0.08936		41	0.08650
	26	0.08879		42	0.08669
	27	0.08828		43	0.08691
	28	0.08783		44	0.08717
	29	0.08745			

4.3. Comparison of the Rational Results of Different Textures

The rational geometric parameter values for all three textures were similarly determined and are presented in Table 5 alongside their friction coefficients.

Table 5 shows that the ellipsoidal cap is the most effective texture among the three in reducing the coefficient of friction of the spherical bearings. Therefore, it is the most favorable surface texture for spherical bearings. The double spherical cap texture has the highest friction coefficient, indicating that this texture is unsuitable for the spherical bearings considered. These results are consistent with reference [41], which reported a friction coefficient of 0.095 for a bridge construction sliding bearing lubricated by silicone grease and subjected to a pressure of 3.5 MPa. This friction coefficient value is slightly higher than the minimum friction coefficient obtained in this study for spherical cap and ellipsoidal cap textures, but slightly lower than the minimum friction coefficient of the double spherical cap. This also implies the reliability of the numerical results in this study.

The lubricant film pressure of the three textures, each with the best geometric parameter values, is displayed in Figure 13a–c, and the maximum lubrication pressure of the three textures is compared in Figure 13d. This clearly shows high similarity between different textures, while the double spherical cap texture exhibits slightly lower maximum lubrication pressure. However, this does not mean that the three textures exhibit similar lubrication performance, because the lubrication pressure significantly relies on the applied external load. To analyze the lubrication performance, the elastic deformation of the PTFE surface, the lubricant film thickness and cavitation need to be discussed.

Table 5. Geometric parameter values and friction coefficients corresponding to the optimal friction performance of each texture.

Texture	Scheme		Friction Coefficient μ
	Dimension Parameters (μm)	Value	
Spherical cap	r d	230 36	0.08615
Ellipsoidal cap	r_a r_b r d	230 230 600 36	0.08610
Double spherical cap	r_1 r_2 d_1 d_2 d_3	230 70 13 3 8	0.11119

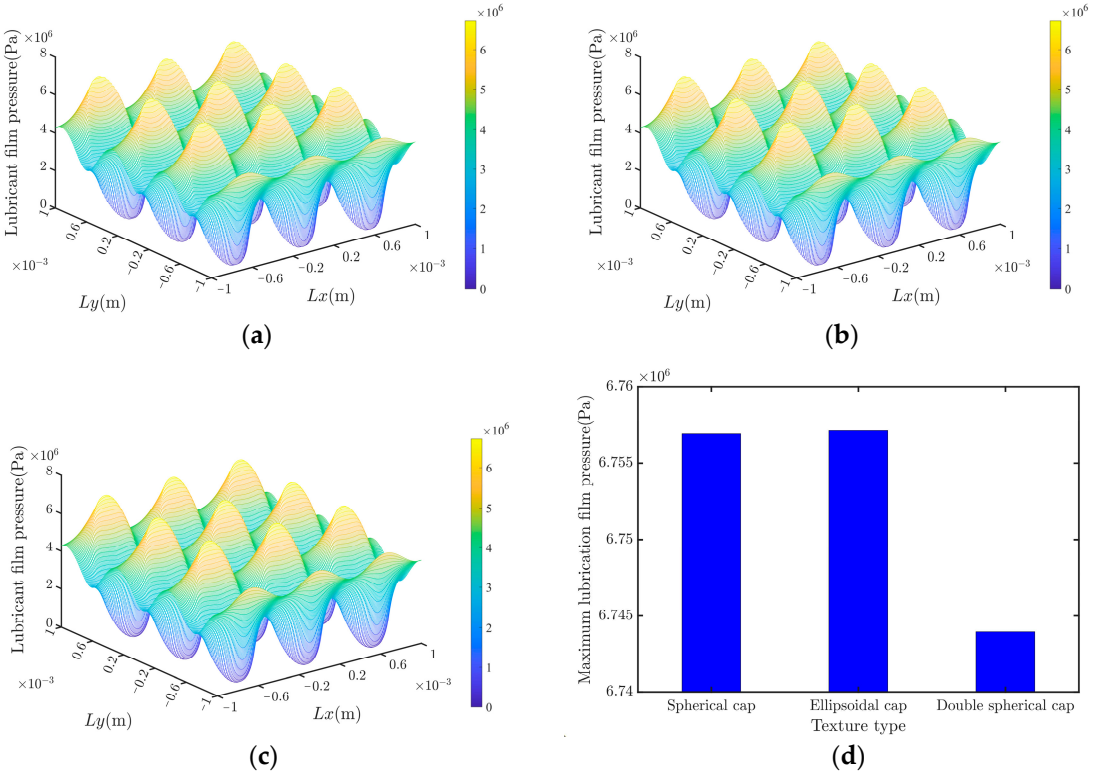


Figure 13. Lubricant film pressure for: (**a**) spherical cap; (**b**) ellipsoidal cap; (**c**) double spherical cap, textures with rational values of their geometric parameters; (**d**) maximum lubricating film pressure of each texture.

The elastic deformation of the three textures, each with the best geometric parameter values, is displayed in Figure 14a–c, while Figure 14d compares the maximum elastic deformation. It can be seen that the elastic deformation of the three textures under the same working conditions reaches 3.75 μm, indicating that the the elastic deformation caused by the lubricant pressure is very important and will significantly affect the lubricant film thickness. It may be noted that the maximum elastic deformation of the ellipsoidal cap texture is slightly smaller than those of the spherical cap and double spherical cap textures, although the ellipsoidal cap and spherical cap textures show similar maximum lubrication pressure, while the double spherical cap texture displays slightly lower maximum lubrication pressure (see Figure 13d). This indicates that different textures affect the load-carrying capability and elastic deformation of the PTFE layer, and such an effect may be severe and non-negligible if the external load is extremely high.

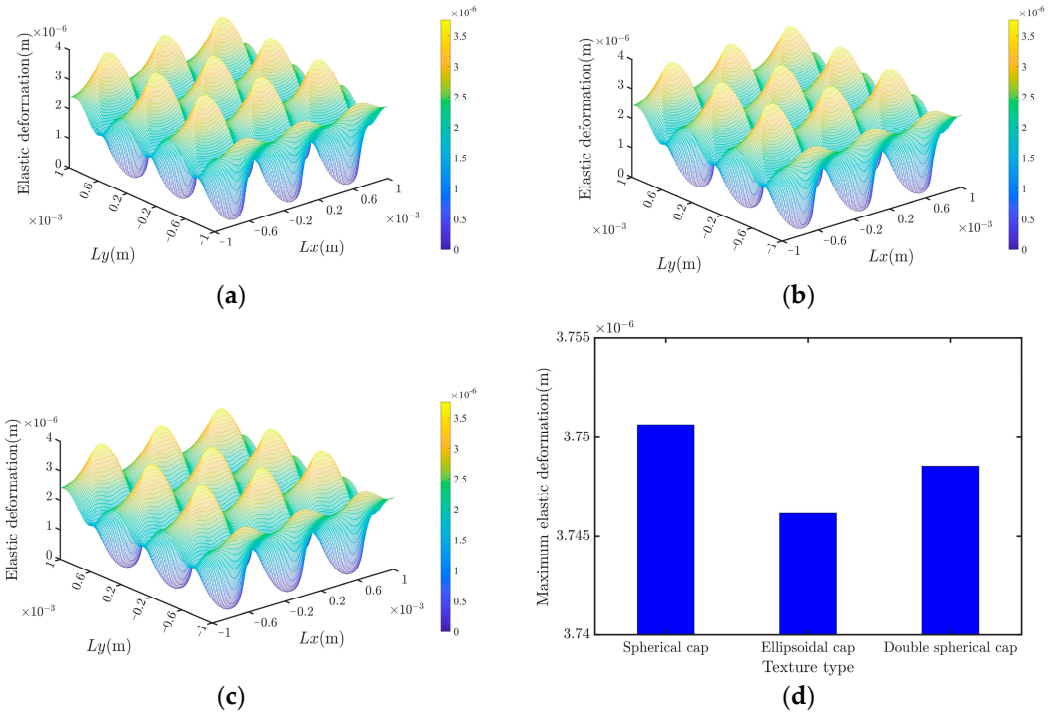


Figure 14. Elastic deformation of the curved PTFE surface in: (**a**) spherical cap; (**b**) ellipsoidal cap; (**c**) double spherical cap, textures with rational values of their geometric parameters; (**d**) maximum elastic deformation of each texture.

Figure 15a–c depict the lubricant film thickness of the three textures, each with the best geometric parameter values, while Figure 15d compares the maximum and minimum lubricant film thicknesses between the three textures. It shows that the spherical and ellipsoidal cap textures lead to a larger maximum lubricant film thickness compared to the double spherical cap texture, while the minimum lubricant film thicknesses of all three textures are almost the same. A larger maximum lubricant film thickness is generally more favorable in actual applications because it means more space to capture microparticles to reduce wear.

Apart from that, Figure 15a–c also show that the gradient of lubricant film thickness of the first two textures is much higher than that of the double spherical cap texture, which may imply that the first two textures are likely to cause severer cavitation. This is validated by Figure 16, which presents the density ratio of the lubricant film. It clearly shows that the former two textures exhibit lower minimum density ratio, i.e., severer cavitation, compared to the double spherical cap texture. In this study, the minimum density ratios for all three textures are close to one, i.e., cavitation is negligible, which may be because the relative sliding velocity between the lubricated surfaces is low. Hence, it can be concluded that the ellipsoidal cap texture is the rational texture since it leads to the minimum friction coefficient. However, in other actual applications where the cavitation becomes severe, one may need to consider the results of the density ratio together with the friction coefficient.

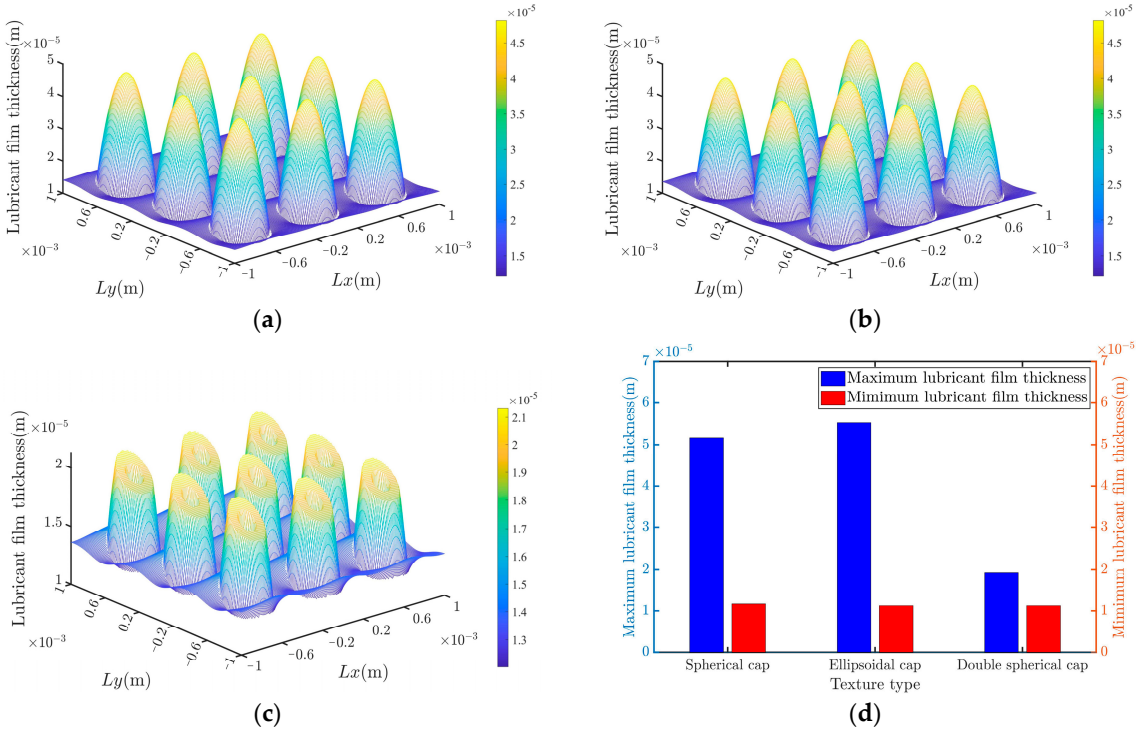


Figure 15. Lubricant film thickness of: (**a**) spherical cap; (**b**) ellipsoidal cap; (**c**) double spherical cap, textures with rational values of their geometric parameters; (**d**) maximum and minimum lubricant film thicknesses of each texture.

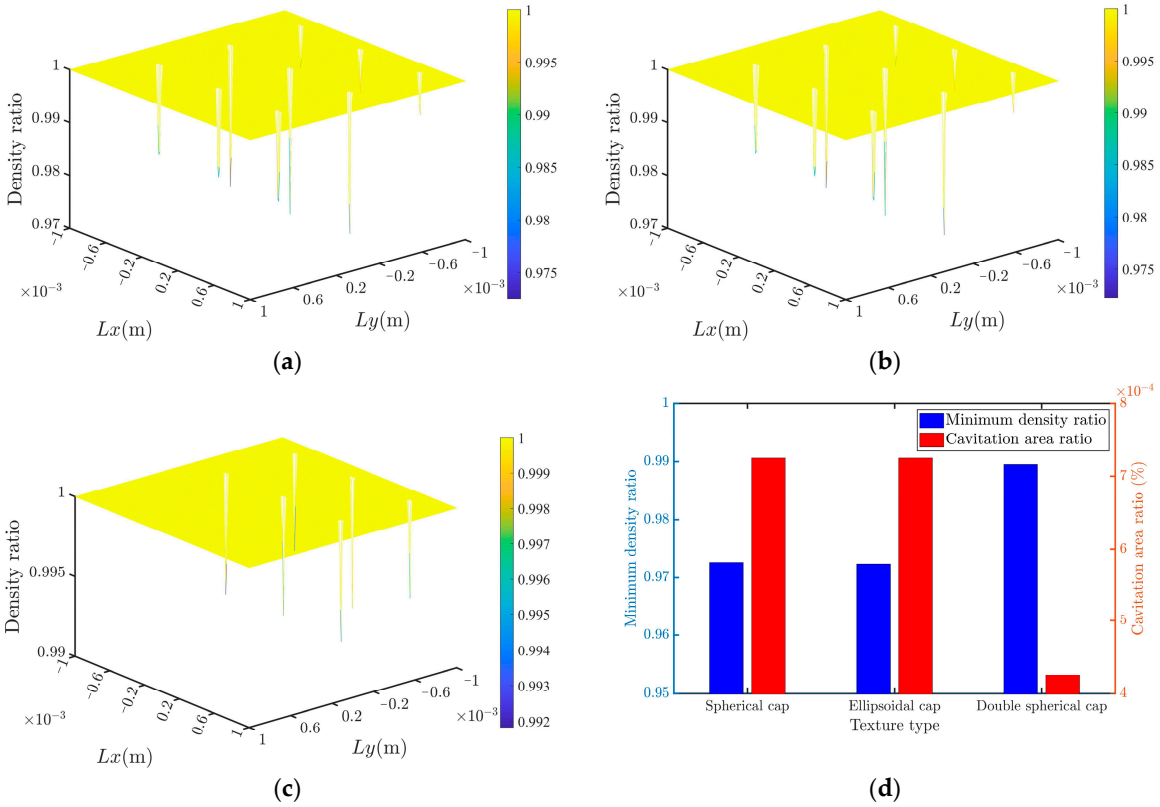


Figure 16. Density ratio of the lubricant film for: (**a**) spherical cap; (**b**) ellipsoidal cap; (**c**) double spherical cap, textures with rational values of their geometric parameters; (**d**) minimum density ratio and cavitation area ratio of each texture.

5. Conclusions

To reduce the friction coefficient of heavy-load GQZ-60000 spherical bearings for bridges, three surface textures, namely spherical cap, ellipsoidal cap, and double spherical cap were introduced to the curved PTFE surface. Based on the Winkler model, the Reynolds equation with the JFO cavitation boundary condition was solved to obtain the elastohydrodynamic lubrication pressure, which further derives the friction coefficient. The effect of geometric parameters of the surface textures on the friction coefficient was analyzed to determine the rational values of parameters as well as the rational textures. Simulation results show that the ellipsoidal cap texture leads to the minimum friction coefficient, which is slightly lower than that of the spherical cap texture. The double spherical cap texture results in a larger friction coefficient. Moreover, in applications where the sliding velocity of lubricated surfaces is high, cavitation effects must be considered. The simulation results indicate that the double spherical cap texture produces less cavitation than the other two textures, which may be advantageous in high-speed applications where cavitation-induced film rupture can degrade lubrication performance.

This study, based on numerical simulations and theoretical analysis, demonstrates the effectiveness of surface textures in improving lubrication performance. However, three key limitations remain: (1) the lack of experimental validation, which will be addressed in future studies; (2) the assumption of a uniformly distributed load, whereas real-world bridge spherical bearings experience dynamic loading conditions; and (3) the absence of explicit analysis on edge effects, which may influence hydrodynamic lubricant film distribution and pressure variation. Future work will incorporate experimental studies, consider complex loading conditions, and assess edge effects to further refine the proposed model.

Author Contributions: Conceptualization, Q.H., Q.P. and P.L.; methodology, Q.P. and P.L.; software, Q.H. and Q.P.; validation, Q.H. and Q.P.; formal analysis, Q.H. and Q.P.; investigation, Q.H. and Q.P.; resources, P.L.; data curation, Q.H. and Q.P.; writing—original draft preparation, Q.P.; writing—review and editing, P.L.; visualization, Q.P.; supervision, P.L.; project administration, P.L.; funding acquisition, P.L. All authors have read and agreed to the published version of the manuscript.

Funding: This research was funded by the National Key Research and Development Program of China (2022YFB4601700).

Data Availability Statement: The data presented in this study are available on request from the corresponding author.

Conflicts of Interest: The authors declare no conflicts of interest.

References

1. *GB/T 17955-2009*; Spherical Bearings for Bridges. Standardization Administration of China: Beijing, China, 2009; p. 20.
2. Huang, Y.; Zhao, C.; Liu, K. Research on the application of ceramic coating technology in friction pairs of bridge supports. *Constr. Mach. Equip.* **2024**, *55*, 29-35+8.
3. Zhang, B. A High Stability Bridge Spherical Bearing. CN213804859U, 27 July 2021.
4. Wang, L. The Tribological Property Design and Study of High-Speed Railway Bridge Isolation Spherical Bearings. Master's Thesis, University of Jinan, Jinan, China, 2018.
5. Feng, L. Design and performance analysis of steel damping and isolation bearings for railway bridge beams. *Railw. Constr. Technol.* **2023**, *09*, 51–54.
6. Song, L. Research and development of a new type of seismic spherical support for rail transit. *Highway* **2018**, *63*, 76–79.
7. Zhang, H.; Liu, Y.; Wang, W.; Qin, L.; Dong, G. Surface texture design and its tribological application. *J. Mech. Eng.* **2019**, *55*, 85–93.
8. Dykha, O.; Dytyniuk, V.; Kovtun, O.; Fasolia, V.; Hetman, M. Improving the wear resistance of guides: Tribological analysis, surface texture and lubricants. *Probl. Tribol.* **2025**, *30*, 51–59. [CrossRef]
9. Greiner, C.; Merz, T.; Braun, D.; Codrignani, A.; Magagnato, F. Optimum dimple diameter for friction reduction with laser surface texturing: The effect of velocity gradient. *Surf. Topogr. Metrol. Prop.* **2015**, *3*, 044001. [CrossRef]

10. Chen, X.; Huang, Y.; Rong, Y.; Wu, C. Two-step laser processing of micro/nano-composite structures on PS-SiC surfaces for superior friction performance under water-lubrication. *Ceram. Int.* **2025**. [CrossRef]
11. Nakanishi, Y.; Fujiwara, Y.; Nakashima, Y.; Komohara, Y.; Hino, K.; Miura, H.; Higaki, H. Effects of Counterface Surface Texturing on Wear Behaviour of Ultra-High Molecular Weight Polyethylene Used in Artificial Joints. *Tribol. Int.* **2025**, *207*, 110638. [CrossRef]
12. Lu, P.; Wood, R.J.; Gee, M.G.; Wang, L.; Pfleging, W. The friction reducing effect of square-shaped surface textures under lubricated line-contacts—An experimental study. *Lubricants* **2016**, *4*, 26. [CrossRef]
13. Annadi, R.R.; Syed, I. Impact of multi-scaled surface textures on tribological performance of parallel sliding contact under lubricated condition. *Tribol. Int.* **2023**, *183*, 108415. [CrossRef]
14. Guo, J.; Li, C.; Du, Q.; Liu, Y. Fabrication of superhydrophobic AlCrN coatings and their tribological properties under dry and starved lubrication conditions. *Vacuum* **2025**, *238*, 114276. [CrossRef]
15. Liu, C.; Liu, C.; Hu, X.; Yuan, W. The effect of bionic scallop microtexture protrusions on the tribological performance of shot-peened 65Mn steel plow surface. *Ind. Lubr. Tribol.* **2025**. [CrossRef]
16. Gropper, D.; Wang, L.; Harvey, T.J. Hydrodynamic lubrication of textured surfaces: A review of modeling techniques and key findings. *Tribol. Int.* **2016**, *94*, 509–529. [CrossRef]
17. Kovalchenko, A.; Ajayi, O.; Erdemir, A.; Fenske, G.; Etsion, I. The effect of laser texturing of steel surfaces and speed-load parameters on the transition of lubrication regime from boundary to hydrodynamic. *Tribol. Trans.* **2004**, *47*, 299–307. [CrossRef]
18. Xie, Y.; Li, Y.; Wang, Y.; Suo, S.; Liu, X. An experimental investigation of tribological performance of triangular textures in water lubrication regime. *Sci. China Phys. Mech. Astron.* **2014**, *57*, 273–279. [CrossRef]
19. Li, P.; Pei, Q.; Liu, Z.; Luo, S.; Zhou, L.; Li, J.; Chen, L. Parametric Optimization of Surface Textures in Oil-Lubricated Long-Life Aircraft Valves. *Lubricants* **2024**, *12*, 405. [CrossRef]
20. Wang, Z.; Hu, S.; Zhang, H.; Ji, H.; Yang, J.; Liang, W. Effect of surface texturing parameters on the lubrication characteristics of an axial piston pump valve plate. *Lubricants* **2018**, *6*, 49. [CrossRef]
21. Qiu, M.; Delic, A.; Raeymaekers, B. The effect of texture shape on the load-carrying capacity of gas-lubricated parallel slider bearings. *Tribol. Lett.* **2012**, *48*, 315–327. [CrossRef]
22. Hu, S.; Zheng, L.; Guo, Q.; Ren, L. Influence of Cross-Grooved Texture Shape on Tribological Performance under Mixed Lubrication. *Coatings* **2022**, *12*, 305. [CrossRef]
23. Shen, C.; Khonsari, M. Numerical optimization of texture shape for parallel surfaces under unidirectional and bidirectional sliding. *Tribol. Int.* **2015**, *82*, 1–11. [CrossRef]
24. Shen, J.; Zhang, T.; Xu, J.; Liu, X.; Liu, K. Experimental study on friction coefficient and temperature rise of heavy-load grease-lubricated spherical plain bearings with surface texture. *Ind. Lubr. Tribol.* **2021**, *73*, 536–542. [CrossRef]
25. Dang, G.; Zheng, C.; Xiong, C.; Ma, B.; Chen, M.; Luo, D. Influences of Surface Texture on the Friction Characteristics of Powder Metallurgy Clutch Disks. *Tribol. Trans.* **2024**, *67*, 857–874. [CrossRef]
26. Tang, L.; Liu, Y. Influence of surface micro-texture on the tribological properties of heavy-duty gears. *J. Tsinghua Univ. (Nat. Sci. Ed.)* **2010**, *50*, 1009–1012.
27. Liu, Y.; Zhang, H.; Dong, G. A Design of Partial Textured Surface on Gear Washers for Reducing Friction and Wear under Low Speed and Heavy Load Conditions. *Materials* **2021**, *14*, 4666. [CrossRef] [PubMed]
28. Dong, B.; Liu, X.; Wang, J.; Liu, K. Effect of textured surface on the frictional property of 40Cr steel under high load and line contact. *Tribology* **2016**, *36*, 145–152.
29. Marcus, B. Friction in Elastohydrodynamic Lubrication. Doctoral Dissertation, Luleå Tekniska Universitet, Luleå, Sweden, 2014.
30. Wang, L.; Wang, W.; Wang, H.; Ma, T.; Hu, Y. Numerical analysis on the factors affecting the hydrodynamic performance for the parallel surfaces with microtextures. *J. Tribol.* **2014**, *136*, 021702. [CrossRef]
31. Zhang, K.; Yagi, K. Refined Hydrodynamic Lubrication Model with a High-Accuracy Numerical Algorithm for Starved Lubrication with Free Surfaces. *Tribol. Lett.* **2023**, *71*, 122. [CrossRef]
32. Lian, H.; Li, X.; Qu, Y.; Du, J.; Meng, Z.; Liu, J.; Chen, L. Bayesian uncertainty analysis for underwater 3D reconstruction with neural radiance fields. *Appl. Math. Model.* **2025**, *138*, 115806. [CrossRef]
33. Chen, L.; Huo, R.; Lian, H.; Yu, B.; Zhang, M.; Natarajan, S.; Bordas, S.P.A. Uncertainty quantification of 3D acoustic shape sensitivities with generalized nth-order perturbation boundary element methods. *Comput. Methods Appl. Mech. Eng.* **2025**, *433*, 117464. [CrossRef]
34. Chen, L.; Liu, C.; Lian, H.; Gu, W. Electromagnetic scattering sensitivity analysis for perfectly conducting objects in TM polarization with isogeometric BEM. *Eng. Anal. Bound. Elem.* **2025**, *172*, 106126. [CrossRef]
35. Chen, L.; Lian, H.; Liu, C.; Li, Y.; Natarajan, S. Sensitivity analysis of transverse electric polarized electromagnetic scattering with isogeometric boundary elements accelerated by a fast multipole method. *Appl. Math. Model.* **2025**, *141*, 115956. [CrossRef]
36. Chen, L.; Pei, Q.; Fei, Z.; Zhou, Z.; Hu, Z. Deep-neural-network-based framework for the accelerating uncertainty quantification of a structural–acoustic fully coupled system in a shallow sea. *Eng. Anal. Bound. Elem.* **2025**, *171*, 106112. [CrossRef]

37. Chen, L.; Lian, H.; Pei, Q.; Meng, Z.; Jiang, S.; Dong, H.-W.; Yu, P. FEM-BEM analysis of acoustic interaction with submerged thin-shell structures under seabed reflection conditions. *Ocean Eng.* **2024**, *309*, 118554. [CrossRef]
38. Zhang, Y.; Wang, M.; Gao, X.; Gao, P.; Yang, X.; Cui, X. Study on the Lubrication and Anti-Friction Characteristics of the Textured Raceway of the Ball Screws Based on Elastohydrodynamic Lubrication. *Appl. Sci.* **2025**, *15*, 3343. [CrossRef]
39. Wen, A.; Zhang, Z.; Yu, S. Analysis of mixed elastohydrodynamic lubrication based on low speed heavy duty rack and pinion transmission mechanism. *Mech. Des. Res.* **2019**, *35*, 85–90+95.
40. Li, P. Investigation of Multibody Systems with Clearance Joints Based on Coupling Dynamics with Tribology. Master's Thesis, Xi'an Jiaotong University, Xi'an, China, 2015.
41. Dorafshan, S.; Johnson, K.R.; Maguire, M.; Halling, M.W.; Barr, P.J.; Culmo, M. Friction coefficients for slide-in bridge construction using PTFE and steel sliding bearings. *J. Bridge Eng.* **2019**, *24*, 04019045. [CrossRef]

Disclaimer/Publisher's Note: The statements, opinions and data contained in all publications are solely those of the individual author(s) and contributor(s) and not of MDPI and/or the editor(s). MDPI and/or the editor(s) disclaim responsibility for any injury to people or property resulting from any ideas, methods, instructions or products referred to in the content.